

Waveguide-Integrated PdSe₂ Photodetector over a Broad Infrared Wavelength Range

Jianghong Wu,[#] Hui Ma,[#] Chuyu Zhong,[#] Maoliang Wei, Chunlei Sun, Yuting Ye, Yan Xu, Bo Tang, Ye Luo, Boshu Sun, Jialing Jian, Hao Dai, Hongtao Lin,^{*} and Lan Li^{*}



Cite This: <https://doi.org/10.1021/acs.nanolett.2c02099>



Read Online

ACCESS |



Metrics & More



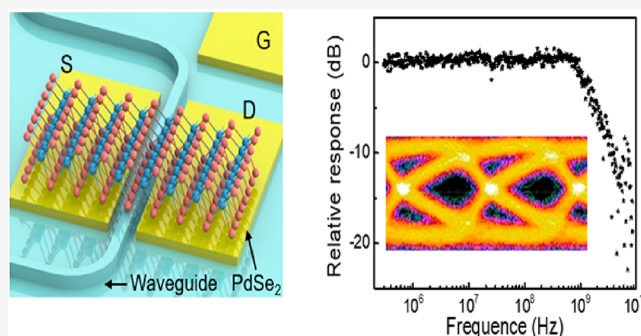
Article Recommendations



Supporting Information

ABSTRACT: Hybrid integration of van der Waals materials on a photonic platform enables diverse exploration of novel active functions and significant improvement in device performance for next-generation integrated photonic circuits, but developing waveguide-integrated photodetectors based on conventionally investigated transition metal dichalcogenide materials at the full optical telecommunication bands and mid-infrared range is still a challenge. Here, we integrate PdSe₂ with silicon waveguide for on-chip photodetection with a high responsivity from 1260 to 1565 nm, a low noise-equivalent power of 4.0 pW·Hz^{-0.5}, a 3-dB bandwidth of 1.5 GHz, and a measured data rate of 2.5 Gbit·s⁻¹. The achieved PdSe₂ photodetectors provide new insights to explore the integration of novel van der Waals materials with integrated photonic platforms and exhibit great potential for diverse applications over a broad infrared range of wavelengths, such as on-chip sensing and spectroscopy.

KEYWORDS: Waveguide-integrated photodetector, PdSe₂, van der Waals materials, Integrated photonics, Infrared



Integrated photonics has been a promising technology widely used in data communications and has gradually established a range of emerging applications in the area of sensing,¹ spectrometer,² light detection and ranging (LiDAR),³ biological research,⁴ and artificial skins.⁵ To meet the functional requirements of various applications, integrated photonic systems consisting of multiple materials, including silicon,⁶ III–V semiconductors,⁷ lithium niobate,⁸ silicon nitride,⁹ polymers,¹⁰ and amorphous glass,¹¹ have been proposed and developed. As one of the essential components in an integrated photonic circuit, the waveguide-integrated photodetector, converting the signal from photons to electrons, is usually constructed by integrating extrinsic materials on an integrated photonic platform. Currently, monolithic integration of germanium films on silicon is the most common strategy for waveguide-integrated photodetectors, but the threading dislocations and surface roughness at the interface are inevitable as the result of the 4.2% lattice mismatch between silicon and germanium, which need to be optimized by complex procedures. Furthermore, the demanding requirements for epitaxial growth make it difficult to integrate germanium with other photonic platforms based on silicon nitride, polymer, and amorphous glass. In contrast, van der Waals materials (VDWMs) are compatible with arbitrary substrates, overcoming the integration limitation induced by the variation of lattice constants and thermal expansion coefficients of each material platform.

Over the past decades, VDWMs have demonstrated intriguing optoelectronic properties, including ultrafast mobility, broadband absorption, and a dangling-bond-free surface, exhibiting great potential for optoelectronic devices.^{12–18} Currently, integrating VDWMs with various integrated photonic platforms has already been realized, and a plethora of prototypical waveguide-integrated photodetectors have been developed.^{19–24} Among all VDWMs, graphene has been extensively studied for waveguide-integrated photodetectors, but graphene photodetectors suffer from a large dark current because of a zero bandgap. Although graphene photodetectors based on photothermoelectric effect (PTE) can work without bias voltage, they usually need a complex device structure such as local doping to obtain the different Seebeck coefficients.¹⁹ VDW semiconductors such as black phosphorus (BP), MoTe₂ and Bi₂O₂Se are alternative candidates.^{25–28} However, the air-unstability of BP limits the applications, and a large optical bandgap for MoTe₂ (1.04 eV) and Bi₂O₂Se (0.9 eV) prevents them from optical detection at the C-band and mid-infrared (MIR) region.

Received: May 25, 2022

Revised: June 29, 2022



ACS Publications

© XXXX American Chemical Society

A

<https://doi.org/10.1021/acs.nanolett.2c02099>
Nano Lett. XXXX, XXX, XXX–XXX

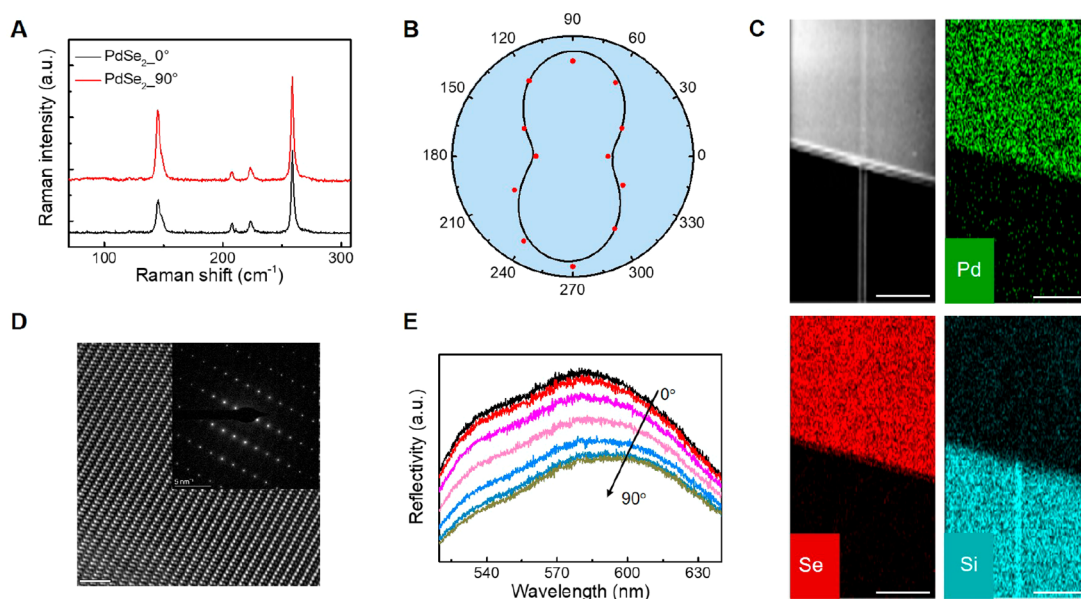


Figure 1. Multilayer PdSe₂ flake characterization. (A) Raman spectra of a multilayer PdSe₂ excited by incident light at 532 nm under two different polarization states. (B) Polar plots of the measured and fitted peak intensities of the A_1^g mode. (C) The energy-dispersive X-ray spectroscopy (EDS) mappings of a multilayer PdSe₂ flake on an SOI ridge waveguide. Scale bar: 5 μm . (D) High-resolution transmission electron microscope (TEM) image of a multilayer PdSe₂ film. The illustration is the corresponding selected area electron diffraction (SAED) pattern. Scale bar: 2 nm. (E) Reflection spectra of a multilayer PdSe₂ flake with a white light source under different polarization states.

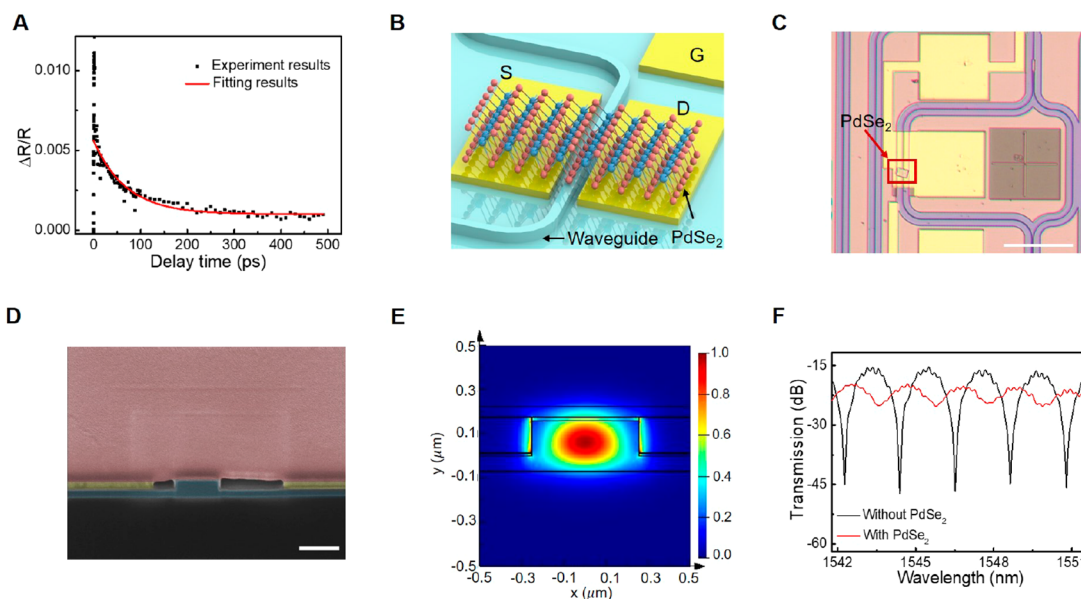


Figure 2. PdSe₂ photodetector integrated with a silicon photonic circuit. (A) Measured ultrafast transient reflectance of a multilayer PdSe₂ flake (12 nm thick). (B) Three-dimensional illustration of the waveguide-integrated PdSe₂ photodetector. (C) Optical image of a PdSe₂ waveguide-integrated photodetector. Scale bar: 100 μm . (D) Cross-section scanning electron microscope (SEM) image of a PdSe₂ photodetector. Blue region is Si waveguide, brown region is PdSe₂, yellow region is Au electrode. Scale bar: 500 nm. (E) Calculated electric field profiles of the TE₀ mode in the hybrid silicon/PdSe₂ waveguide; the thickness of the PdSe₂ flake is 50 nm. (F) Transmission spectra of the unbalanced MZI with and without a PdSe₂ flake (155 nm thick).

Recently, PdSe₂ with great air-stability and a large bandgap tunability, ranging from 0.03 eV (bulk) to ~ 1.3 eV (monolayer) has been a new candidate for optoelectronic applications at NIR and MIR.^{29–32} Moreover, a wafer-scale PdSe₂ can be obtained by a simple selenization process of the predeposited Pd film,^{33,34} and a centimeter-scale PdSe₂ can be prepared by chemical vapor deposition method,³⁵ which ensures the fabrication of a device array. To date, free-space PdSe₂ photodetectors have already been investigated. For

example, a PdSe₂ phototransistor showed photoresponse ranging from the visible to MIR with a slow response time.³⁶ The VDW heterostructure, such as InSe/PdSe₂ and PdSe₂/MoS₂ showed photoresponse at NIR and MIR, but the rise/fall times were tens of milliseconds.^{37,38} Up to now, realizing a PdSe₂ photodetector with high responsivity and large bandwidth is still a challenge and highly desired. Indeed, a waveguide architecture is attractive for designing photodetectors with both high responsivity and large bandwidth. It

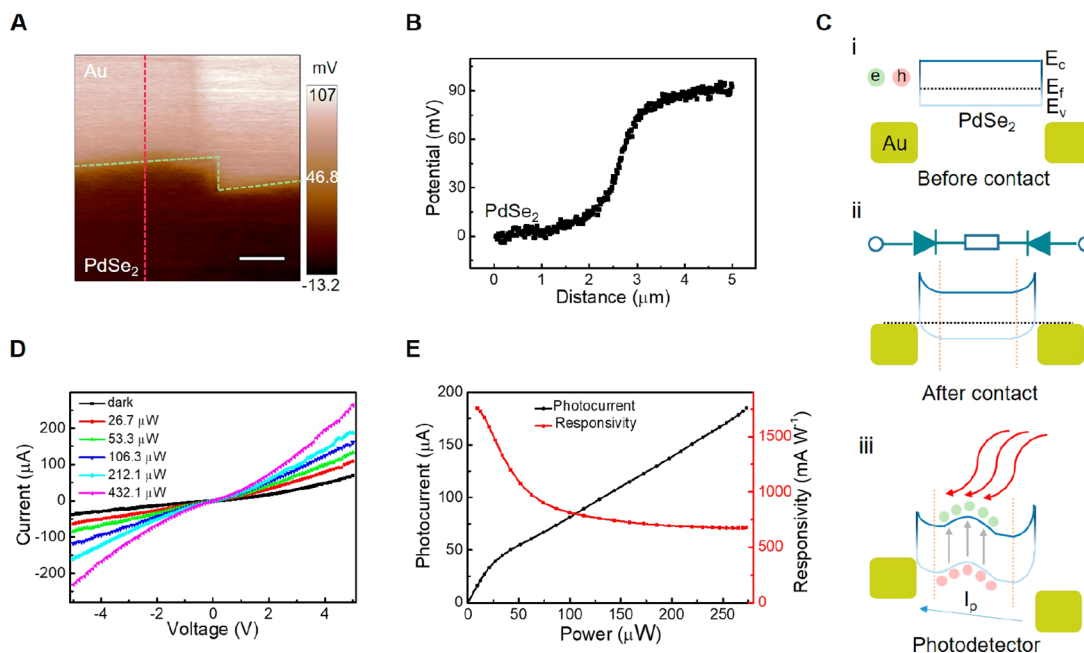


Figure 3. Electronic characteristics of PdSe₂ photodetector. (A) Kelvin probe force microscopy (KPFM) image of the Au-PdSe₂ contact on a Si/SiO₂ substrate, where the green dot line is the edge of the PdSe₂ flake and Au electrode. Scale bar: 1 μm. (B) KPFM profile along with the red dashed line in part A. (C) Energy band diagram of Au-PdSe₂-Au junction at equilibrium, under illumination, at a bias voltage, and corresponding equivalent circuits. (D) Current–voltage (IV) curves a waveguide-integrated PdSe₂ photodetector (Sample 1, S1) in the dark and under illumination with different optical power at 1550 nm. (E) Photocurrent and responsivity versus incident optical power at 5 V.

can simultaneously ensure adequate absorption via evanescent field coupling over a long propagation distance and decrease the transit time of photoinduced carriers with a short channel.

In this work, we proposed and demonstrated waveguide-integrated PdSe₂ photodetectors operating in the telecom optical bands ranging from the O-band to the C-band. The significant optoelectronic properties of multilayer PdSe₂, including anisotropy and ultrafast carrier dynamics, were characterized. We integrated silicon-on-insulator (SOI) ridge waveguides with the multilayer PdSe₂ which were exfoliated from bulk materials and transferred by an imprint-transfer process. Such devices ensure sufficient optical absorption for the fundamental mode of TE polarization (TE₀). The present PdSe₂ waveguide-integrated photodetectors possess a broadband spectral operation, a high responsivity of 1758.7 mA·W⁻¹, and a low noise-equivalent power (NEP) of 4.0 pW·Hz^{-0.5} at 1550 nm (5 V). Additionally, a 3-dB bandwidth reaches up to 1.5 GHz, and the eye diagram indicates PdSe₂ photodetector could realize a data transmission rate being more than 2.5 Gbit·s⁻¹.

Raman spectra of a multilayer PdSe₂ flake on SiO₂ substrate are shown in Figure 1A, where four distinct Raman peaks at about 143, 206, 222, and 256 cm⁻¹ are observed, which are corresponding to A_g¹, A_g², B_{1g}², and A_g³ modes, respectively. Furthermore, the measured Raman spectra under different polarization states show the strong in-plane anisotropic phonon vibration (Figure S1A). The polarization-dependent Raman intensity of A_g¹–B_{1g}¹ (Figure 1B) shows clear periodical variations of π . The chemical composition of multilayer PdSe₂ was characterized by X-ray photoelectron spectroscopy (XPS) measurement (Figure S1) in which four typical peaks at 54.6, 55.4, 336.7, and 342.1 eV are ascribed to Se 3d_{5/2}, 3d_{3/2}, Pd 3d_{5/2}, and 3d_{3/2} orbitals, respectively. The EDS mappings of a multilayer PdSe₂ flake on an SOI ridge waveguide are shown in

Figure 1C, where Pd and Se elements show a uniform distribution. Moreover, the high-magnification TEM image and SAED pattern in Figure 1D demonstrate the single-crystal characteristic of the exfoliated multilayer PdSe₂ flake. Additionally, anisotropic optical properties were confirmed by the variation of the reflection spectra under different polarization states (Figure 1E), and the reflectivity decreases gradually when the polarization angle increases from 0° to 90°, which indicates that the crystal orientation has an impact on photon-to-electron transition.

The lifetime of photoinduced carriers was inferred by the ultrafast transient reflectance (TR) spectroscopy. We excited a multilayer PdSe₂ flake with a 2.07 eV pump pulse (50 fs pulse duration) and measured the reflectance change using a white-light continuum probe. The TR kinetics (Figure 2A) indicates that the lifetime of photoinduced carriers of this PdSe₂ flake (12 nm thick in Figure S1D) is about 68 ps. With the thickness increase, a narrowing bandgap induces a shorter lifetime of photoinduced carriers, and the measured lifetime under 1550 nm wavelength illumination is 22 ps for a multilayer PdSe₂ flake (20 nm thick) in the previous report.³⁹ The lifetime is longer than that counterpart of graphene,⁴⁰ indicating PdSe₂ photodetectors can not only realize a high photoconductive gain ($G = \tau_{\text{lif}}/\tau_{\text{tran}}$, τ_{tran} is the drift transit time), but also a large 3-dB bandwidth.

Figure 2B shows the schematic configuration, where SOI ridge waveguide (220 nm thick) with an etching height of 150 nm is applied. The silicon waveguide was lightly doped, and the heavily doped area (2×10^{20} cm⁻³) was close to the waveguide at a suitable distance. The Al₂O₃ film (15 nm thick) was deposited to avoid photoinduced carriers transferring between a PdSe₂ flake and the Si waveguide. Two Ti/Au pads (5/100 nm) were deposited and placed around the straight waveguide, and a PdSe₂ flake was transferred to the top of a

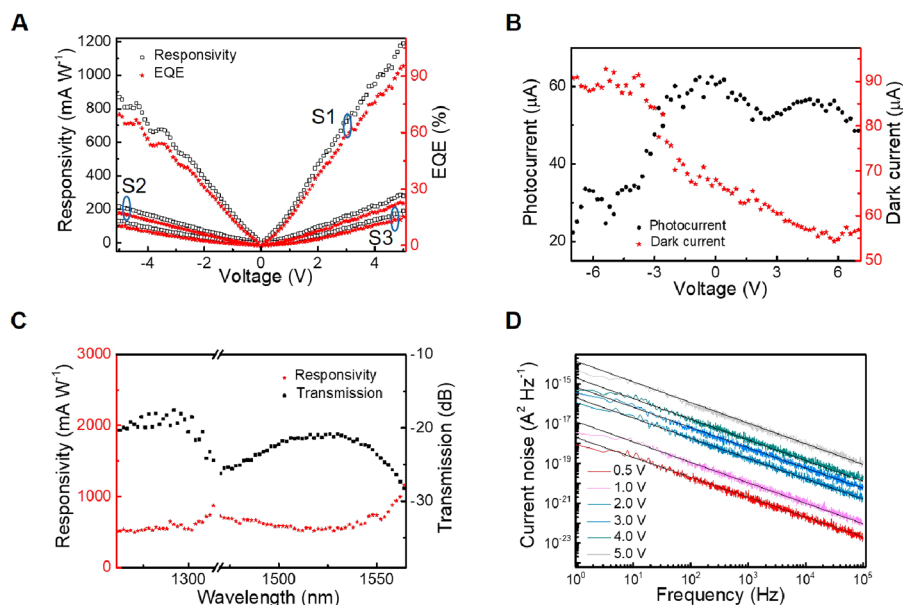


Figure 4. Static performance of PdSe₂ photodetectors. (A) Responsivity and EQE for S1, S2, and S3 at different bias voltage under the illumination of 1550 nm. (B) Gate-tunable transport and photoresponse of a PdSe₂ photodetector (S1), the optical power is 42 μ W. (C) Spectral response of PdSe₂ photodetectors (the measured results at O-band are obtained by S4, and others are obtained by S1). (D) $1/f$ noise spectra of a waveguide-integrated PdSe₂ photodetector (S1) under different applied voltages. The black lines show the best fitting of the test results.

waveguide. Incident light was coupled into/out waveguide by two grating couplers whose SEM images are illustrated in Figure S2. The detailed process of device fabrication is shown in Supporting Information. A typical optical image of the waveguide-integrated PdSe₂ photodetector is shown in Figure 2C, where a PdSe₂ flake is on one arm of an unbalanced Mach–Zehnder interferometer (MZI). The cross-section SEM image of a waveguide-integrated PdSe₂ photodetector (Figure 2D) indicates that an altitude difference remains at the top of the waveguide core, slab and Au pads, and a part of the PdSe₂ flake is suspended. The adhesion between a PdSe₂ flake and the waveguide substrate was strong enough, which has been verified in subsequent experiments.

The simulated electric field profile of the TE₀ mode indicates that PdSe₂ can not only realize optical absorption at 1550 nm but also avoid a high mode-mismatching loss (Figure 2E). The experimental optical absorption was characterized by comparing the transmission spectra of an unbalanced MZI (Figure 2F) with/without a PdSe₂ flake. In this unbalanced MZI, beam splitter and combiner are realized by two 1×2 MMIs. The detailed performance of a 1×2 MMI (Figure S3) indicates that it splits incident light power equally. According to the change of extinction ratio (ER), the absorption coefficient of the PdSe₂ (155 nm thick)/Si hybrid waveguide is calculated to be 0.14 dB/ μ m at 1550 nm. We also demonstrated the transmission spectra variation of a straight waveguide with/without a PdSe₂ flake (Figure S9A). Actually, the slight difference in grating couplers during different operations leads to an experimental error in the absorption coefficient of the PdSe₂/Si hybrid waveguide, which could be avoided by measuring from an MZI.

Next, we measured the contact potential difference (V_{CPD}) between an Au electrode and a PdSe₂ flake by KPFM. The KPFM image of a PdSe₂–Au junction (Figure 3A) indicates the different work functions for an Au electrode and a PdSe₂ flake, and the detailed surface potential profile along the red dot line (Figure 3B) shows that the work function difference is

about 90 meV. The smaller work function results in electron transferring from PdSe₂ flake to Au electrode, with an upward sloping of the energy band, and a built-in electric field at the contact interface. Therefore, the equivalent circuit can be regarded as a back-to-back Schottky junction (Figure 3C). The photovoltaic effect (PVE) is usually dominant for free-space photodetectors based on Au–semiconductor–Au structure. However, the optical absorption of a PdSe₂ flake is mainly located on top of a waveguide surface (Figure 2E), and the distance between the Au electrode and optical absorption area is larger than the width of the depletion area. Thereby, photocurrent at 0 V is extremely weak in this photodetector, similar to waveguide-integrated photodetector based on BP.²⁷ Moreover, the weak photocurrent at 0 V excludes PTE effect as well. Additionally, photobolometric effect is also eliminated because the photocurrent increases nonlinearly with the bias voltage.⁴¹

The static characteristics of a PdSe₂ photodetector (sample1) were measured, and IV curves in the dark and under illumination at 1550 nm were demonstrated (Figure 3D). The nonlinear property of IV curves is attributed to a Schottky barrier at the contact interface between Au and PdSe₂, which is primarily attributed to two aspects. On the one hand, a low background doping level of the multilayer PdSe₂ flake⁴² brings about a large depletion layer width. On the other hand, a multilayer PdSe₂ flake was transferred onto the Au electrode, avoiding unnecessary chemical disorder and Fermi-level pinning, leading to a better Schottky junction.⁴³ The dark current is $-38 \mu\text{A}$ at -5 V , with the PdSe₂ thickness of 139 nm (Figure S5), which decreases with the thinner thickness.⁴⁴ Furthermore, aligning the crystal orientation has an impact on dark current,⁴⁵ approved by the anisotropic electronic transport (Figure S6), which provides flexibility to the device design. The photocurrent–incident optical power curve (Figure 3E) at 5 V shows the nonlinear property at the small optical power, which is primarily attributed to the low-lying, long-lived traps in PdSe₂. In the future, a larger linear dynamic range can

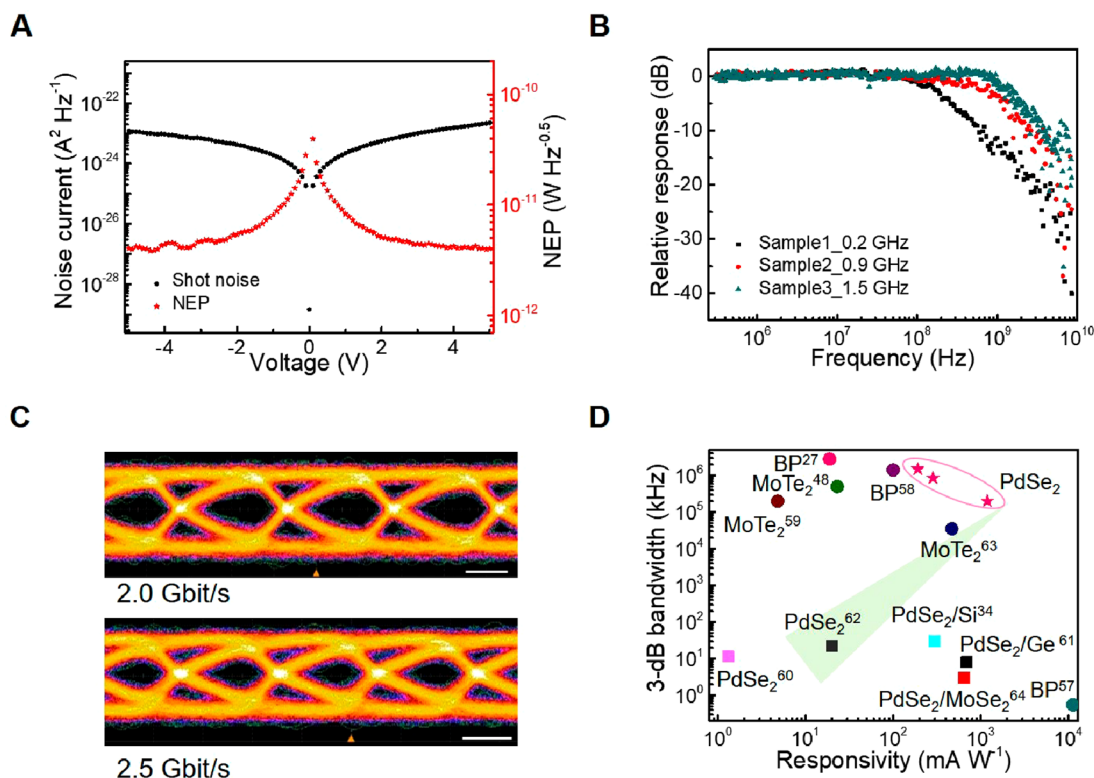


Figure 5. Dynamic performance of PdSe₂ photodetectors. (A) NEP and noise current induced by shot noise at different bias voltage. (B) Measured frequency response of three PdSe₂ photodetectors (S1, S2 and S3) at 3 V. (C) Receiver eye diagram at a data rate of 2.0 and 2.5 Gbit s⁻¹ measured with a PdSe₂ photodetector (S3). Scale bar: 200 ps. (D) Summary of the performance for waveguide-integrated photodetectors (circular shapes) based on VDW semiconductors and free-space photodetectors (rectangular shapes) based on PdSe₂ flakes. Three five-pointed stars represent waveguide-integrated photodetectors (S1, S2, and S3). The green arrow indicates the direction of device with improved performance.

be obtained by growing the high-quality PdSe₂ without trap states.

Responsivity varies as a function of bias voltage (Figure 4A) because the higher efficiency of the generation-separation-collection process of photoinduced carriers can be realized at a larger bias voltage. The external responsivity ($R = I_p/P_{in}$) is 1190.2, 285.7, and 191.2 mA·W⁻¹ at 5 V and 1550 nm for S1, S2, and S3, respectively, and the external quantum efficiency ($EQE = 1.24 \times R/\lambda$) is 95.2%, 22.9%, and 15.3%, where λ is the incident light wavelength. Such an external responsivity and EQE are higher than the counterparts based on graphene,^{46,47} BP,²⁷ and MoTe₂.⁴⁸ The variation of responsivities for these three samples (S1, S2, and S3) is mainly attributed to the thickness, length, and optical anisotropy of the multilayer PdSe₂ flakes. The exact sizes of PdSe₂ are listed in Table S1. Moreover, the reflectivity varies under different polarization states (Figure 1E), illustrating that optical anisotropy has a severe impact on the optical absorption and the photo-to-electron transition, which is consistent with previous reports.^{49,50} Additionally, responsivity is affected by different PdSe₂ thicknesses (Figure S7). When the PdSe₂ thickness is less than 5.3 nm, the photon-to-electron transition limited by a large optical bandgap is extremely weak, and the PdSe₂ thickness is expected to be thicker than 11.8 nm for efficient optical absorption at 1550 nm.

I_d – V_g curve (Figure 4B) in the dark shows a small on–off ratio for a PdSe₂ photodetector (S1), indicating the PdSe₂ flake is p-doped, which is consistent with previous reports.⁴² The thickness of the PdSe₂ flake (139 nm thick) is significantly greater than the Debye screening length, resulting in the device

not being thoroughly turned off and a moderate gate-dependent transport. Another two PdSe₂ field-effect transistors on a SiO₂/Si substrate also verify the gate-dependent transport (Figure S8). The transport indicates that multilayer PdSe₂ flake possesses a low background doping because the onset of different doping locates about $V_g = 0$ V. Moreover, the gate-dependent photocurrent is primarily attributed to the variation of optical absorption of PdSe₂ flakes (Figure 4B), rather than the larger thermionic and tunneling currents,⁵¹ being similar to graphene photodetectors.⁵² As shown in Figure 2D, carrier variation induced by a back-gate voltage mainly concentrates on the area at the top surface of a waveguide; thereby, a back-gate voltage has little impact on the PdSe₂–Au Schottky barriers, as well as thermionic and tunneling currents. Similar results, including the unipolar dark current and maximal photocurrent at $V_g = 0$ V were observed in another waveguide-integrated photodetector as well (Figure S9).

The spectral photoresponse (Figure 4C) demonstrates the broadband operation of PdSe₂ photodetectors, and the responsivity is more than 500 mA·W⁻¹ with input optical power being larger than 200 μW at 5 V. Limited by a finite optical bandwidth of grating couplers, we fabricated two photodetectors (S1 and S4) to show this broadband spectral photoresponse. One photodetector (S4) works at O-band, corresponding to the responsivity at wavelengths from 1260 to 1325 nm, and the detailed characteristics of S4 are illustrated (Figure S10). Another photodetector (S1) works at wavelengths from 1470 to 1565 nm. The fluctuating responsivity is attributed to the incident power variation at different wavelengths. During this measurement, since the output

power of the laser at different wavelengths was fixed, the practical incident power passing through the waveguide at different wavelengths was different due to various coupling efficiencies of the grating couplers. A smaller incident power usually brings about a large photocurrent gain and responsivity; thereby, the responsivity at the wavelengths with a weak coupling efficiency is higher, which is consistent with the measured result in Figure 3E. Furthermore, the operational wavelengths of PdSe₂ photodetectors can be extended to MIR as well. The photocurrent of free-space PdSe₂ photodetectors with illumination at 2 μm can be observed in Figure S4.

Moreover, we analyzed the noise-equivalent power (NEP = i_n/R) of the PdSe₂ photodetectors, where i_n is the noise current. The measured $1/f$ noise spectral density in Figure 4D indicates that PdSe₂ photodetectors possess typical characteristics of $1/f$ noise, which can be determined by the Hooge's empirical relationship ($S_i = A \cdot i_n^\alpha / f^\beta$),^{53,54} where i , f , and A are the channel current, the frequency, and the noise amplitude, respectively. β is fitted to be 1.0, 1.03, 1.02, 1.02, 1.04, and 1.04 for bias voltages at 0.5, 1.0, 2.0, 3.0, 4.0, and 5.0 V. Moreover, the current noise induced by the shot noise and the thermal noise are evaluated to be 2.24×10^{-23} and 2.32×10^{-25} A²Hz⁻¹ at 5.0 V. Usually, the $1/f$ noise dominates at a small frequency,⁵⁴ but the measured $1/f$ noise is much larger than the shot noise at 10^5 Hz. The origin of such a high $1/f$ noise in the PdSe₂ photodetector probably results from the fluctuating occupancy of trap states which enlarges the fluctuation of carrier density, leading to the $1/f$ -spectra extending over a higher frequency.⁵⁵ The remaining trap states in PdSe₂ are confirmed by the obvious photocurrent gain at low optical power. Assuming that β is an invariant constant when the $1/f$ noise is larger than the shot noise, the turning point of white noise is about 700 MHz, and NEP is estimated to be 4.0 pW·Hz^{-0.5} at 5 V. Furthermore, the current noise for a PdSe₂ photodetector increases with the applied voltage, but a smaller NEP is obtained at the larger bias voltage (Figure 5A). This phenomenon is attributed to the fact that a larger bias voltage brings about a higher efficiency of the separation-collection process of photogenerated carriers and a larger responsivity.

The measured 3-dB bandwidths for S1, S2, and S3 are about 0.2, 0.9, and 1.5 GHz, respectively (Figure 5B), whose measurement setup is shown in Figure S11. The total response time is determined by the carrier with a transit time (τ_{tr}) and the charge/discharge time of the junction capacitance (τ_{RC}). The τ_{tr} can be written as $\tau_{tr} = \frac{l^2}{2\mu V_{DS}}$, where l , μ , V_{DS} are the length of a PdSe₂ photodetector, the mobility of a PdSe₂ flake, and the bias voltage, respectively. Mobility of PdSe₂ was measured to be 216 cm²·V⁻¹·s⁻¹,⁵⁶ the calculated τ_{tr} is about 29 ps (5.3 GHz) at 5 V. However, the measured 3-dB bandwidths remained almost at the same value for S3 (Figure S12), indicating that total response time (τ) is determined by τ_{RC} . Impedance matching in measurement is necessary for a PdSe₂ photodetector with larger bandwidth in the future. Additionally, we performed an eye-diagram measurement to illustrate the feasibility of PdSe₂ photodetectors for receiving high bit-rate data. The experimental results (Figure 5C) demonstrate a completely open eye at 3 V with a data rate of 2.5 Gbit·s⁻¹. Overall, the proposed PdSe₂ photodetectors show apparent advantages compared with photodetectors based on VDW semiconductors (Figure S2),^{27,34,48,57–64} and the detailed comparison is listed in Supporting Information.

In summary, we have realized integrated photodetectors based on SOI ridge waveguides and multilayer PdSe₂ covering the datacom and telecom wavelength range (1260–1565 nm). The obtained photodetectors possessed a high responsivity of 1758.7 mA·W⁻¹ at 1550 nm, a 3-dB bandwidth of 1.5 GHz, a data rate being more than 2.5 Gbit·s⁻¹, and a NEP of about 4.0 pW·Hz^{-0.5}. In the future, the 3-dB bandwidth can be optimized by both reducing the contact resistance between PdSe₂ flakes and metal electrodes and shortening the channel length. Overall, these results pave the way for integrating PdSe₂ flake onto an integrated photonic platform and provide a new route to integrated photodetectors for applications in diverse areas, including optical communications, on-chip spectroscopy, and sensing.

■ ASSOCIATED CONTENT

Supporting Information

The Supporting Information is available free of charge at <https://pubs.acs.org/doi/10.1021/acs.nanolett.2c02099>.

Additional results and details for waveguide-integrated photodetector fabrication and measurement, multilayer PdSe₂ flakes characterization, SEM and performance of the passive integrated device, photoresponse of free-space PdSe₂ photodetector at 2 μm , AFM results for PdSe₂, characterization of the anisotropic electronic transport property, gate-dependent transport properties measurement, static photoresponse, dynamic measurement setups, and dynamic response of S3 under different bias voltages (PDF)

■ AUTHOR INFORMATION

Corresponding Authors

Lan Li – Key Laboratory of 3D Micro/Nano Fabrication and Characterization of Zhejiang Province, School of Engineering, Westlake University, Hangzhou 310024, China; Institute of Advanced Technology, Westlake Institute for Advanced Study, Hangzhou 310024, China; orcid.org/0000-0002-9097-9157; Email: lilan@westlake.edu.cn

Hongtao Lin – State Key Laboratory of Modern Optical Instrumentation, College of Information Science and Electronic Engineering, Zhejiang University, Hangzhou 310027, China; MOE Frontier Science Center for Brain Science & Brain-Machine Integration, Zhejiang University, Hangzhou 310027, China; orcid.org/0000-0001-7432-3644; Email: hometown@zju.edu.cn

Authors

Jianghong Wu – State Key Laboratory of Modern Optical Instrumentation, College of Information Science and Electronic Engineering, Zhejiang University, Hangzhou 310027, China; Key Laboratory of 3D Micro/Nano Fabrication and Characterization of Zhejiang Province, School of Engineering, Westlake University, Hangzhou 310024, China; Institute of Advanced Technology, Westlake Institute for Advanced Study, Hangzhou 310024, China

Hui Ma – State Key Laboratory of Modern Optical Instrumentation, College of Information Science and Electronic Engineering, Zhejiang University, Hangzhou 310027, China; MOE Frontier Science Center for Brain Science & Brain-Machine Integration, Zhejiang University, Hangzhou 310027, China

Chuyu Zhong – State Key Laboratory of Modern Optical Instrumentation, College of Information Science and Electronic Engineering, Zhejiang University, Hangzhou 310027, China; MOE Frontier Science Center for Brain Science & Brain-Machine Integration, Zhejiang University, Hangzhou 310027, China

Maoliang Wei – State Key Laboratory of Modern Optical Instrumentation, College of Information Science and Electronic Engineering, Zhejiang University, Hangzhou 310027, China; MOE Frontier Science Center for Brain Science & Brain-Machine Integration, Zhejiang University, Hangzhou 310027, China

Chunlei Sun – Key Laboratory of 3D Micro/Nano Fabrication and Characterization of Zhejiang Province, School of Engineering, Westlake University, Hangzhou 310024, China; Institute of Advanced Technology, Westlake Institute for Advanced Study, Hangzhou 310024, China

Yuting Ye – Key Laboratory of 3D Micro/Nano Fabrication and Characterization of Zhejiang Province, School of Engineering, Westlake University, Hangzhou 310024, China; Institute of Advanced Technology, Westlake Institute for Advanced Study, Hangzhou 310024, China

Yan Xu – Key Laboratory of 3D Micro/Nano Fabrication and Characterization of Zhejiang Province, School of Engineering, Westlake University, Hangzhou 310024, China; Institute of Advanced Technology, Westlake Institute for Advanced Study, Hangzhou 310024, China

Bo Tang – Institute of Microelectronics, Chinese Academic Society, Beijing 100029, China

Ye Luo – Key Laboratory of 3D Micro/Nano Fabrication and Characterization of Zhejiang Province, School of Engineering, Westlake University, Hangzhou 310024, China; Institute of Advanced Technology, Westlake Institute for Advanced Study, Hangzhou 310024, China

Boshu Sun – State Key Laboratory of Modern Optical Instrumentation, College of Information Science and Electronic Engineering, Zhejiang University, Hangzhou 310027, China; MOE Frontier Science Center for Brain Science & Brain-Machine Integration, Zhejiang University, Hangzhou 310027, China

Jialing Jian – Key Laboratory of 3D Micro/Nano Fabrication and Characterization of Zhejiang Province, School of Engineering, Westlake University, Hangzhou 310024, China; Institute of Advanced Technology, Westlake Institute for Advanced Study, Hangzhou 310024, China

Hao Dai – State Key Laboratory of Modern Optical Instrumentation, College of Information Science and Electronic Engineering, Zhejiang University, Hangzhou 310027, China; MOE Frontier Science Center for Brain Science & Brain-Machine Integration, Zhejiang University, Hangzhou 310027, China

Complete contact information is available at:
<https://pubs.acs.org/10.1021/acs.nanolett.2c02099>

Author Contributions

L.L., H.L., and J.W. conceived the project. J.W., H.M., C.Z., M.W., Y.Y., Y.X., B.T., Y.L., B.S., J.J., and H.D. fabricated these devices. J.W., M.W., and C.S. designed the passive optical devices. J.W. performed the optical and optoelectronic measurements. L.L., H.L., and J.W. analyzed the data and wrote the manuscript. All authors commented on the manuscript.

Author Contributions

#J.W., H.M., and C.Z. contributed equally to this work.

Notes

The authors declare no competing financial interest.

ACKNOWLEDGMENTS

The authors thank ZJU Micro-Nano Fabrication Center at Zhejiang University, Westlake Center for Micro/Nano Fabrication and Instrumentation and Service Center for Physical Sciences at Westlake University for the facility support, and Prof. Haiming Zhu and Mr. Cheng Sun for the support of ultrafast transient reflectance measurement. The research was partially supported by the National Key Research and Development Program of China (2019YFB2203003), National Natural Science Foundation of China (Grant Numbers 12104375, 62175202, 61975179 and 91950204), Leading Innovative and Entrepreneur Team Introduction Program of Zhejiang (2020R01005), Zhejiang Provincial Natural Science Foundation of China (LD22F040002) and the Foundation of Key Laboratory of 3D Micro/Nano Fabrication and Characterization of Zhejiang Province, Westlake University.

REFERENCES

- (1) Chen, Y.; Lin, H.; Hu, J.; Li, M. Heterogeneously integrated silicon photonics for the mid-infrared and spectroscopic sensing. *ACS Nano* **2014**, *8*, 6955–6961.
- (2) Le Coarer, E.; Blaize, S.; Benech, P.; Stefanon, I.; Morand, A.; Lérondel, G.; Leblond, G.; Kern, P.; Fedeli, J. M.; Royer, P. Wavelength-scale stationary-wave integrated Fourier-transform spectrometry. *Nat. Photonics* **2007**, *1*, 473–478.
- (3) Zhang, X.; Kwon, K.; Henriksson, J.; Luo, J.; Wu, M. C. A large-scale microelectromechanical-systems-based silicon photonics LiDAR. *Nature* **2022**, *603*, 253–258.
- (4) Mohanty, A.; Li, Q.; Tadayon, M. A.; Roberts, S. P.; Bhatt, G. R.; Shim, E.; Ji, X.; Cardenas, J.; Miller, S. A.; Kepecs, A.; et al. Reconfigurable nanophotonic silicon probes for sub-millisecond deep-brain optical stimulation. *Nat. Biomed. Eng.* **2020**, *4*, 223–231.
- (5) Zhang, L.; Pan, J.; Zhang, Z.; Wu, H.; Yao, N.; Cai, D.; Xu, Y.; Zhang, J.; Sun, G.; Wang, L.; et al. Ultrasensitive skin-like wearable optical sensors based on glass micro/nanofibers. *Opto-Electron. Adv.* **2020**, *3*, 19002201–19002207.
- (6) Soref, R. The past, present, and future of silicon photonics. *IEEE J. Sel. Top. Quantum Electron.* **2006**, *12*, 1678–1687.
- (7) Roelkens, G.; Liu, L.; Liang, D.; Jones, R.; Fang, A.; Koch, B.; Bowers, J. III-V/silicon photonics for on-chip and intra-chip optical interconnects. *Laser Photonics Rev.* **2010**, *4*, 751–779.
- (8) Zhu, D.; Shao, L.; Yu, M.; Cheng, R.; Desiatov, B.; Xin, C.; Hu, Y.; Holzgrafe, J.; Ghosh, S.; Shams-Ansari, A.; et al. Integrated photonics on thin-film lithium niobate. *Adv. Opt. Photonics* **2021**, *13*, 242–352.
- (9) Liang, G.; Huang, H.; Mohanty, A.; Shin, M. C.; Ji, X.; Carter, M. J.; Shrestha, S.; Lipson, M.; Yu, N. Robust, efficient, micrometre-scale phase modulators at visible wavelengths. *Nat. Photonics* **2021**, *15*, 908–913.
- (10) Dangel, R.; Hofrichter, J.; Horst, F.; Jubin, D.; La Porta, A.; Meier, N.; Soganci, I. M.; Weiss, J.; Offrein, B. J. Polymer waveguides for electro-optical integration in data centers and high-performance computers. *Opt. Express* **2015**, *23*, 4736–4750.
- (11) Li, L.; Lin, H.; Qiao, S.; Huang, Y.-Z.; Li, J.-Y.; Michon, J.; Gu, T.; Alosno-Ramos, C.; Vivien, L.; Yadav, A.; et al. Monolithically integrated stretchable photonics. *Light-Sci. Appl.* **2018**, *7*, 17138–17138.
- (12) Wu, J.; Ma, H.; Yin, P.; Ge, Y.; Zhang, Y.; Li, L.; Zhang, H.; Lin, H. Two-Dimensional Materials for Integrated Photonics: Recent Advances and Future Challenges. *Small Science* **2021**, *1*, 2000053.

- (13) Rezaei, M.; Bianconi, S.; Lauhon, L. J.; Mohseni, H. A New Approach to Designing High-Sensitivity Low-Dimensional Photo-detectors. *Nano Lett.* **2021**, *21*, 9838–9844.
- (14) Takeyama, K.; Moriya, R.; Okazaki, S.; Zhang, Y. J.; Masubuchi, S.; Watanabe, K.; Taniguchi, T.; Sasagawa, T.; Machida, T. Resonant Tunneling Due to van der Waals Quantum-Well States of Few-Layer WSe₂ in WSe₂/h-BN/p⁺-MoS₂ Junction. *Nano Lett.* **2021**, *21*, 3929–3934.
- (15) Lv, L.; Yu, J.; Hu, M.; Yin, S. M.; Zhuge, F. W.; Ma, Y.; Zhai, T. Y. Design and tailoring of two-dimensional Schottky, PN and tunnelling junctions for electronics and optoelectronics. *Nanoscale* **2021**, *13*, 6713–6751.
- (16) Zou, Z. X.; Li, D.; Liang, J. W.; Zhang, X. H.; Liu, H. W.; Zhu, C. G.; Yang, X.; Li, L. H.; Zheng, B. Y.; Sun, X. X.; Zeng, Z. X. S.; Yi, J. L.; Zhuang, X. J.; Wang, X.; Pan, A. L. Epitaxial synthesis of ultrathin beta-In₂Se₃/MoS₂ heterostructures with high visible/near-infrared photoresponse. *Nanoscale* **2020**, *12*, 6480–6488.
- (17) Sun, Z.; Martinez, A.; Wang, F. Optical modulators with 2D layered materials. *Nat. Photonics* **2016**, *10*, 227–238.
- (18) Wu, J.; Lu, Y.; Feng, S.; Wu, Z.; Lin, S.; Hao, Z.; Yao, T.; Li, X.; Zhu, H.; Lin, S. The Interaction between Quantum Dots and Graphene: The Applications in Graphene-Based Solar Cells and Photodetectors. *Adv. Funct. Mater.* **2018**, *28*, 1804712.
- (19) Mišeikis, V.; Marconi, S.; Giambra, M. A.; Montanaro, A.; Martini, L.; Fabbri, F.; Pezzini, S.; Piccinini, G.; Forti, S.; Terrés, B.; Goykhman, I.; Hamidouche, L.; Legagneux, P.; Soriano, V.; Ferrari, A. C.; Koppens, F. H. L.; Romagnoli, M.; Coletti, C. Ultrafast, Zero-Bias, Graphene Photodetectors with Polymeric Gate Dielectric on Passive Photonic Waveguides. *ACS Nano* **2020**, *14*, 11190–11204.
- (20) Ma, Y.; Chang, Y.; Dong, B.; Wei, J.; Liu, W.; Lee, C. Heterogeneously Integrated Graphene/Silicon/Halide Waveguide Photodetectors toward Chip-Scale Zero-Bias Long-Wave Infrared Spectroscopic Sensing. *ACS Nano* **2021**, *15*, 10084–10094.
- (21) Gan, X.; Shiue, R.-J.; Gao, Y.; Meric, I.; Heinz, T. F.; Shepard, K.; Hone, J.; Assefa, S.; Englund, D. Chip-integrated ultrafast graphene photodetector with high responsivity. *Nat. Photonics* **2013**, *7*, 883–887.
- (22) Wang, X.; Cheng, Z.; Xu, K.; Tsang, H. K.; Xu, J.-B. High-responsivity graphene/silicon-heterostructure waveguide photodetectors. *Nat. Photonics* **2013**, *7*, 888–891.
- (23) Shiue, R.-J.; Gao, Y.; Wang, Y.; Peng, C.; Robertson, A. D.; Efetov, D. K.; Assefa, S.; Koppens, F. H.; Hone, J.; Englund, D. High-responsivity graphene-boron nitride photodetector and autocorrelator in a silicon photonic integrated circuit. *Nano Lett.* **2015**, *15*, 7288–7293.
- (24) Goykhman, I.; Sassi, U.; Desiatov, B.; Mazurski, N.; Milana, S.; De Fazio, D.; Eiden, A.; Khurgin, J.; Shappir, J.; Levy, U.; et al. On-chip integrated, silicon-graphene plasmonic Schottky photodetector with high responsivity and avalanche photogain. *Nano Lett.* **2016**, *16*, 3005–3013.
- (25) Wu, J.; Wei, M.; Mu, J.; Ma, H.; Zhong, C.; Ye, Y.; Sun, C.; Tang, B.; Wang, L.; Li, J.; Xu, X.; Liu, B.; Li, L.; Lin, H. High-Performance Waveguide-Integrated Bi₂O₃Se Photodetector for Si Photonic Integrated Circuits. *ACS Nano* **2021**, *15*, 15982–15991.
- (26) Flöry, N.; Ma, P.; Salamin, Y.; Emboras, A.; Taniguchi, T.; Watanabe, K.; Leuthold, J.; Novotny, L. Waveguide-integrated van der Waals heterostructure photodetector at telecom wavelengths with high speed and high responsivity. *Nat. Nanotechnol.* **2020**, *15*, 118–124.
- (27) Youngblood, N.; Chen, C.; Koester, S. J.; Li, M. Waveguide-integrated black phosphorus photodetector with high responsivity and low dark current. *Nat. Photonics* **2015**, *9*, 247–252.
- (28) Yin, Y.; Cao, R.; Guo, J.; Liu, C.; Li, J.; Feng, X.; Wang, H.; Du, W.; Qadir, A.; Zhang, H.; Ma, Y.; Gao, S.; Xu, Y.; Shi, Y.; Tong, L.; Dai, D. High-Speed and High-Responsivity Hybrid Silicon/Black-Phosphorus Waveguide Photodetectors at 2 μ m. *Laser Photonics Rev.* **2019**, *13*, 1900032.
- (29) Cheng, P. K.; Tang, C. Y.; Ahmed, S.; Qiao, J. P.; Zeng, L. H.; Tsang, Y. H. Utilization of group 10 2D TMDs-PdSe₂ as a nonlinear optical material for obtaining switchable laser pulse generation modes. *Nanotechnology* **2021**, *32*, 055201.
- (30) Luo, L. B.; Wang, D.; Xie, C.; Hu, J. G.; Zhao, X. Y.; Liang, F. X. PdSe₂ Multilayer on Germanium Nanocones Array with Light Trapping Effect for Sensitive Infrared Photodetector and Image Sensing Application. *Adv. Funct. Mater.* **2019**, *29*, 1900849.
- (31) Sun, J.; Shi, H.; Siegrist, T.; Singh, D. J. Electronic, transport, and optical properties of bulk and mono-layer PdSe₂. *Appl. Phys. Lett.* **2015**, *107*, 153902.
- (32) Oyedele, A. D.; Yang, S.; Liang, L.; Poretzky, A. A.; Wang, K.; Zhang, J.; Yu, P.; Pudasaini, P. R.; Ghosh, A. W.; Liu, Z.; Rouleau, C. M.; Sumpter, B. G.; Chisholm, M. F.; Zhou, W.; Rack, P. D.; Geohagan, D. B.; Xiao, K. PdSe₂: Pentagonal Two-Dimensional Layers with High Air Stability for Electronics. *J. Am. Chem. Soc.* **2017**, *139*, 14090–14097.
- (33) Liang, F.-X.; Zhao, X.-Y.; Jiang, J.-J.; Hu, J.-G.; Xie, W.-Q.; Lv, J.; Zhang, Z.-X.; Wu, D.; Luo, L.-B. Light Confinement Effect Induced Highly Sensitive, Self-Driven Near-Infrared Photodetector and Image Sensor Based on Multilayer PdSe₂/Pyramid Si Heterojunction. *Small* **2019**, *15*, 1903831.
- (34) Zeng, L.-H.; Wu, D.; Lin, S.-H.; Xie, C.; Yuan, H.-Y.; Lu, W.; Lau, S. P.; Chai, Y.; Luo, L.-B.; Li, Z.-J.; Tsang, Y. H. Controlled Synthesis of 2D Palladium Diselenide for Sensitive Photodetector Applications. *Adv. Funct. Mater.* **2019**, *29*, 1806878.
- (35) Wei, M.; Lian, J.; Zhang, Y.; Wang, C.; Wang, Y.; Xu, Z. Layer-dependent optical and dielectric properties of centimeter-scale PdSe₂ films grown by chemical vapor deposition. *NPJ. 2D Mater. Appl.* **2022**, *6*, 1–8.
- (36) Liang, Q. J.; Wang, Q. X.; Zhang, Q.; Wei, J. X.; Lim, S. X. D.; Zhu, R.; Hu, J. X.; Wei, W.; Lee, C.; Sow, C.; Zhang, W. J.; Wee, A. T. S. High-Performance, Room Temperature, Ultra-Broadband Photodetectors Based on Air-Stable PdSe₂. *Adv. Mater.* **2019**, *31*, 1807609.
- (37) Long, M.; Wang, Y.; Wang, P.; Zhou, X.; Xia, H.; Luo, C.; Huang, S.; Zhang, G.; Yan, H.; Fan, Z.; Wu, X.; Chen, X.; Lu, W.; Hu, W. Palladium Diselenide Long-Wavelength Infrared Photodetector with High Sensitivity and Stability. *ACS Nano* **2019**, *13*, 2511–2519.
- (38) Ahmad, W.; Liu, J.; Jiang, J.; Hao, Q.; Wu, D.; Ke, Y.; Gan, H.; Laxmi, V.; Ouyang, Z.; Ouyang, F.; Wang, Z.; Liu, F.; Qi, D.; Zhang, W. Strong Interlayer Transition in Few-Layer InSe/PdSe₂ van der Waals Heterostructure for Near-Infrared Photodetection. *Adv. Funct. Mater.* **2021**, *31*, 2104143.
- (39) Ye, C.; Yang, Z.; Dong, J.; Huang, Y.; Song, M.; Sa, B.; Zheng, J.; Zhan, H. Layer-Tunable Nonlinear Optical Characteristics and Photocarrier Dynamics of 2D PdSe₂ in Broadband Spectra. *Small* **2021**, *17*, 2103938.
- (40) Sun, D.; Wu, Z.-K.; Divin, C.; Li, X.; Berger, C.; de Heer, W. A.; First, P. N.; Norris, T. B. Ultrafast relaxation of excited Dirac fermions in epitaxial graphene using optical differential transmission spectroscopy. *Phys. Rev. Lett.* **2008**, *101*, 157402.
- (41) Long, M.; Wang, P.; Fang, H.; Hu, W. Progress, Challenges, and Opportunities for 2D Material Based Photodetectors. *Adv. Funct. Mater.* **2019**, *29*, 1803807.
- (42) Zhang, G.; Amani, M.; Chaturvedi, A.; Tan, C.; Bullock, J.; Song, X.; Kim, H.; Lien, D.-H.; Scott, M. C.; Zhang, H.; Javey, A. Optical and electrical properties of two-dimensional palladium diselenide. *Appl. Phys. Lett.* **2019**, *114*, 253102.
- (43) Liu, Y.; Guo, J.; Zhu, E.; Liao, L.; Lee, S.-J.; Ding, M.; Shakir, I.; Gambin, V.; Huang, Y.; Duan, X. Approaching the Schottky-Mott limit in van der Waals metal-semiconductor junctions. *Nature* **2018**, *557*, 696–700.
- (44) Xie, C.; Jiang, S.; Gao, Y.; Hong, M.; Pan, S.; Zhao, J.; Zhang, Y. Giant Thickness-Tunable Bandgap and Robust Air Stability of 2D Palladium Diselenide. *Small* **2020**, *16*, 2000754.
- (45) Li, P.; Zhang, J.; Zhu, C.; Shen, W.; Hu, C.; Fu, W.; Yan, L.; Zhou, L.; Zheng, L.; Lei, H.; Liu, Z.; Zhao, W.; Gao, P.; Yu, P.; Yang, G. Penta-PdPSe: A New 2D Pentagonal Material with Highly In-Plane Optical, Electronic, and Optoelectronic Anisotropy. *Adv. Mater.* **2021**, *33*, 2102541.

(46) Shiue, R.-J.; Gao, Y.; Wang, Y.; Peng, C.; Robertson, A. D.; Efetov, D. K.; Assefa, S.; Koppens, F. H. L.; Hone, J.; Englund, D. High-Responsivity Graphene-Boron Nitride Photodetector and Autocorrelator in a Silicon Photonic Integrated Circuit. *Nano Lett.* **2015**, *15*, 7288–7293.

(47) Schuler, S.; Schall, D.; Neumaier, D.; Dobusch, L.; Bethge, O.; Schwarz, B.; Krall, M.; Mueller, T. Controlled Generation of a p-n Junction in a Waveguide Integrated Graphene Photodetector. *Nano Lett.* **2016**, *16*, 7107–7112.

(48) Ma, P.; Flöry, N.; Salamin, Y.; Baeuerle, B.; Emboras, A.; Josten, A.; Taniguchi, T.; Watanabe, K.; Novotny, L.; Leuthold, J. Fast MoTe₂ Waveguide Photodetector with High Sensitivity at Telecommunication Wavelengths. *ACS Photonics* **2018**, *5*, 1846–1852.

(49) Pi, L.; Hu, C.; Shen, W.; Li, L.; Luo, P.; Hu, X.; Chen, P.; Li, D.; Li, Z.; Zhou, X.; et al. Highly In-Plane Anisotropic 2D PdSe₂ for Polarized Photodetection with Orientation Selectivity. *Adv. Funct. Mater.* **2021**, *31*, 2006774.

(50) Wu, D.; Jia, C.; Shi, F.; Zeng, L.; Lin, P.; Dong, L.; Shi, Z.; Tian, Y.; Li, X.; Jie, J. Mixed-dimensional PdSe₂/SiNWA heterostructure based photovoltaic detectors for self-driven, broadband photodetection, infrared imaging and humidity sensing. *J. Mater. Chem. A* **2020**, *8*, 3632–3642.

(51) Lopez-Sanchez, O.; Lembke, D.; Kayci, M.; Radenovic, A.; Kis, A. Ultrasensitive photodetectors based on monolayer MoS₂. *Nat. Nanotechnol.* **2013**, *8*, 497–501.

(52) Youngblood, N.; Anugrah, Y.; Ma, R.; Koester, S. J.; Li, M. Multifunctional graphene optical modulator and photodetector integrated on silicon waveguides. *Nano Lett.* **2014**, *14*, 2741–2746.

(53) Chen, T.; Bobbert, P. A.; van der Wiel, W. G. 1/f Noise and Machine Intelligence in a Nonlinear Dopant Atom Network. *Small Science* **2021**, *1*, 2000014.

(54) Balandin, A. A. Low-frequency 1/f noise in graphene devices. *Nat. Nanotechnol.* **2013**, *8*, 549–555.

(55) Wolf, D. *Noise in Physical Systems: Proceedings of the Fifth International Conference on Noise, Bad Nauheim, Fed. Rep. of Germany, March 13–16, 1978*; Springer Science & Business Media: 2013; Vol. 2.

(56) Chow, W. L.; Yu, P.; Liu, F.; Hong, J.; Wang, X.; Zeng, Q.; Hsu, C.-H.; Zhu, C.; Zhou, J.; Wang, X.; Xia, J.; Yan, J.; Chen, Y.; Wu, D.; Yu, T.; Shen, Z.; Lin, H.; Jin, C.; Tay, B. K.; Liu, Z. High Mobility 2D Palladium Diselenide Field-Effect Transistors with Tunable Ambipolar Characteristics. *Adv. Mater.* **2017**, *29*, 1602969.

(57) Ma, Y.; Dong, B.; Wei, J.; Chang, Y.; Huang, L.; Ang, K. W.; Lee, C. High-Responsivity Mid-Infrared Black Phosphorus Slow Light Waveguide Photodetector. *Adv. Opt. Mater.* **2020**, *8*, 2000337.

(58) Tian, R.; Gu, L.; Ji, Y.; Li, C.; Chen, Y.; Hu, S.; Li, Z.; Gan, X.; Zhao, J. Black Phosphorus Photodetector Enhanced by a Planar Photonic Crystal Cavity. *ACS Photonics* **2021**, *8*, 3104–3110.

(59) Bie, Y.-Q.; Grosso, G.; Heuck, M.; Furchi, M. M.; Cao, Y.; Zheng, J.; Bunandar, D.; Navarro-Moratalla, E.; Zhou, L.; Efetov, D. K.; et al. A MoTe₂-based light-emitting diode and photodetector for silicon photonic integrated circuits. *Nat. Nanotechnol.* **2017**, *12*, 1124–1129.

(60) Li, G.; Yin, S.; Tan, C.; Chen, L.; Yu, M.; Li, L.; Yan, F. Fast Photothermoelectric Response in CVD-Grown PdSe₂ Photodetectors with In-Plane Anisotropy. *Adv. Funct. Mater.* **2021**, *31*, 2104787.

(61) Wu, D.; Guo, J.; Du, J.; Xia, C.; Zeng, L.; Tian, Y.; Shi, Z.; Tian, Y.; Li, X. J.; Tsang, Y. H.; et al. Highly polarization-sensitive, broadband, self-powered photodetector based on graphene/PdSe₂/germanium heterojunction. *ACS Nano* **2019**, *13*, 9907–9917.

(62) Dong, Z.; Yu, W.; Zhang, L.; Mu, H.; Xie, L.; Li, J.; Zhang, Y.; Huang, L.; He, X.; Wang, L.; Lin, S.; Zhang, K. Highly Efficient, Ultraproduct PdSe₂ Phototransistors from Visible to Terahertz Driven by Mutiphysical Mechanism. *ACS Nano* **2021**, *15*, 20403–20413.

(63) Maiti, R.; Patil, C.; Saadi, M. A. S. R.; Xie, T.; Azadani, J. G.; Uluotku, B.; Amin, R.; Briggs, A. F.; Miscuglio, M.; Van Thourhout, D.; Solares, S. D.; Low, T.; Agarwal, R.; Bank, S. R.; Sorger, V. J. Strain-engineered high-responsivity MoTe₂ photodetector for silicon photonic integrated circuits. *Nat. Photonics* **2020**, *14*, 578–584.

(64) Zhong, J.; Wu, B.; Madoune, Y.; Wang, Y.; Liu, Z.; Liu, Y. PdSe₂/MoSe₂ vertical heterojunction for self-powered photodetector with high performance. *Nano Research* **2022**, *15*, 2489–2496.

Recommended by ACS

Waveguide-Integrated van der Waals Heterostructure Mid-Infrared Photodetector with High Performance

Po-Liang Chen, Chang-Hua Liu, *et al.*

APRIL 27, 2022
ACS APPLIED MATERIALS & INTERFACES

READ 

Electrical Control of Interband Resonant Nonlinear Optics in Monolayer MoS₂

Yunyun Dai, Zhipeng Sun, *et al.*

JUNE 29, 2020
ACS NANO

READ 

Giant Piezotronic Effect by Photoexcitation–Electronic Coupling in a p-GaN/AlGaN/GaN Heterojunction

Hong-Quan Nguyen, Dzung Viet Dao, *et al.*

JUNE 08, 2022
ACS APPLIED ELECTRONIC MATERIALS

READ 

Single-Nanowire Thermo-Optic Modulator Based on a Varshni Shift

Zhangxing Shi, Limin Tong, *et al.*

AUGUST 03, 2020
ACS PHOTONICS

READ 

Get More Suggestions >